nature communications

Article

https://doi.org/10.1038/s41467-025-58593-w

Electro-activated indigos intensify ampere-level CO_2 reduction to CO on silver catalysts

Received: 29 October 2024

Accepted: 26 March 2025

Zhengyuan Li[1,10] ✉, Xing Li[1,2,10], Ruoyu Wang[3], Astrid Campos Mata[4], Carter S. Gerke[5], Shuting Xiang[6], Anmol Mathur[1], Lingyu Zhang[1], Dian-Zhao Lin[1], Tianchen Li[1], Krish N. Jayarapu[1], Andong Liu[1], Lavanya Gupta[1], Anatoly I. Frenkel[6,7], V. Sara Thoi[5,8], Pulickel M. Ajayan[4], Soumyabrata Roy[4,9], Yuanyue Liu[3] & Yayuan Liu[1] ✉

The electrochemical reduction of carbon dioxide (CO_2) to carbon monoxide (CO) is challenged by a selectivity decline at high current densities. Here we report a class of indigo-based molecular promoters with redox-active CO_2 binding sites to enhance the high-rate conversion of CO_2 to CO on silver (Ag) catalysts. Theoretical calculations and in situ spectroscopy analyses demonstrate that the synergistic effect at the interface of indigo-derived compounds and Ag nanoparticles could activate CO_2 molecules and accelerate the formation of key intermediates ($^*CO_2^-$ and *COOH) in the CO pathway. Indigo derivatives with electron-withdrawing groups further reduce the overpotential for CO production upon optimizing the interfacial CO_2 binding affinity. By integrating the molecular design of redox-active centres with the defect engineering of Ag structures, we achieve a Faradaic efficiency for CO exceeding 90% across a current density range of $0.10 - 1.20\ \mathrm{A\ cm^{-2}}$. The Ag mass activity toward CO increases to $174\ \mathrm{A\ mg^{-1}}_{\mathrm{Ag}}$. This work showcases that employing redox-active CO_2 sorbents as surface modification agents is a highly effective strategy to intensify the reactivity of electrochemical CO_2 reduction.

The electrocatalytic carbon dioxide reduction reaction (CO_2RR) powered by renewable electricity offers an attractive carbon-negative route for producing industrial chemicals and fuels[1]. Among the various products of CO_2RR, carbon monoxide (CO) stands out as the most competitive target when considering the market value and cost efficiency[2–4]. To render CO_2 electrolysis profitable compared to conventional petrochemical processes, techno-economic analyses indicate that the Faradaic efficiency (FE) for CO should exceed 90% at current densities above 500 mA cm^{-2} (refs 3,4). However, achieving high-rate, high-selectivity CO production in CO_2RR remains challenging, as near-unity selectivity is only observed at limited partial current densities[2]. This limitation arises from the large overpotential required to initiate CO_2 conversion, coupled with the competing hydrogen evolution reaction (HER)[2].

The linear CO_2 molecule features a robust C=O bond of 1.163 Å in length and 750 kJ mol^{-1} in dissociation energy, making it

---

[1]Department of Chemical and Biomolecular Engineering, Johns Hopkins University, Baltimore, MD, USA. [2]Department of Chemistry, City University of Hong Kong, Hong Kong, China. [3]Texas Materials Institute and Department of Mechanical Engineering, The University of Texas at Austin, Austin, TX, USA. [4]Department of Materials Science and NanoEngineering, Rice University, Houston, TX, USA. [5]Department of Chemistry, Johns Hopkins University, Baltimore, MD, USA. [6]Department of Materials Science and Chemical Engineering, Stony Brook University, Stony Brook, NY, USA. [7]Chemistry Division, Brookhaven National Laboratory, Upton, NY, USA. [8]Department of Materials Science and Engineering, Johns Hopkins University, Baltimore, MD, USA. [9]Department of Sustainable Energy Engineering, Indian Institute of Technology Kanpur, Kanpur, Uttar Pradesh, India. [10]These authors contributed equally: Zhengyuan Li, Xing Li. ✉e-mail: zli326@jh.edu; yayuanliu@jhu.edu

thermodynamically stable and difficult to activate[5]. The two-electron, two-proton conversion of CO_2 to CO typically involves the adsorption and activation of CO_2 to form the $*CO_2^-$ intermediate, which is subsequently hydrogenated to produce the carbon-bound *COOH species, followed by further reduction and desorption steps to yield CO (refs. 1,2). The initial activation of CO_2 is demonstrated to be the possible rate-determining step, especially for silver (Ag) catalysts, due to their weak interaction with CO_2 and the sluggish kinetics toward $*CO_2^-$ and *COOH formation[1,6,7]. Therefore, ample efforts have been devoted to promoting CO_2 stabilization and activation on Ag-based catalysts through approaches such as nanostructuring, doping, and alloying[2,8].

Beyond solely tuning metal catalysts, surface modification with organic compounds has emerged as a promising alternative strategy[9,10]. This strategy leverages synergistic effects at the interface between organic molecules and heterogeneous active sites, which regulates the interfacial reactant concentrations, intermediates adsorption, and reaction energy barriers[10]. In this context, compounds exhibiting reactive interactions with CO_2 have been explored for modifying Ag surfaces in CO_2-to-CO conversion[11,12]. For instance, amine-confined Ag has been developed to enrich local CO_2 concentration during oxygen-containing flue gas electro-reduction[13], and grafting pyridine groups onto Ag electrodes has been shown to induce a ten-fold activity enhancement toward CO by stabilizing the *COOH intermediate[14]. Similar improvement has also been observed with Ag catalysts upon the addition of CO_2-binding imidazolium ionic liquids in nonaqueous electrolytes[15]. These studies demonstrate the potential of using organic molecules to modulate the reactivity profiles of heterogeneous CO_2RR. However, a comprehensive understanding of the structure-function relationships in molecularly enhanced catalysts remains elusive, as precise synthetic controls over their interactions with CO_2 and/or relevant intermediates are still lacking[16].

In our recent study, we discovered indigo (Id), a redox-active Lewis base, as an effective CO_2 sorbent for electrochemically mediated carbon capture (Fig. 1a)[17]. Specifically, the carbonyl groups in Id can undergo electro-reduction to form a nucleophilic dianion (Id^{2-}), which then reacts with electrophilic CO_2 to afford a carbonate adduct ($Id\text{-}2CO_2^{2-}$)[17–20]. Inspired by the ability of redox-active Id to capture CO_2 via carbonate formation, we seek to explore the possibility of employing indigo-based compounds as molecular promoters to accelerate CO_2-to-CO conversion in conjunction with Ag catalysts. We envisage that the unique binding interaction between electrochemically reduced Id and CO_2 could facilitate the activation of linear CO_2 molecule into a bent conformation, consequently stabilizing key reaction intermediates to lower the energy barriers for protonation steps[6]. Importantly, molecular engineering allows us to finetune the chemical properties of the CO_2-binding sites, resulting in more favorable intermediate adsorption behaviors[18].

Herein, through a combination of precise molecular design, in situ spectroscopy characterizations, and theoretical calculations, we systematically investigate a series of indigo derivatives with varying CO_2 affinities to unravel the interplay between electro-activated CO_2 sorbents and the catalytic performance at the Ag/organic interface. Moreover, by further immobilizing CO_2-binding moieties into a macromolecular structure and interfacing them with defect-rich Ag particles on a carbon support, the resulting optimized hybrid catalyst markedly improves CO_2RR reactivity and Ag mass activity toward CO. In particular, steady CO FEs of over 90% can be reached at ampere-level current densities up to nearly $1.2\ A\ cm^{-2}$, accompanied by a notable Ag mass activity of $174\ A\ mg^{-1}_{Ag}$ toward CO production.

Results

Probing the promotional effect of indigo on Ag catalyst for CO_2RR toward CO

To confirm the reactivity of reduced Id toward CO_2, we conducted cyclic voltammetry (CV) studies of Id in an aprotic electrolyte under nitrogen (N_2) and CO_2 atmospheres. Analogous to other redox-active CO_2 sorbents, the positive shift in the reduction onset potential and the merging of the two redox waves in the presence of CO_2 strongly imply a chemical interaction between reduced Id and CO_2 (Fig. 1b)[17–20]. The formation of the $Id\text{-}2CO_2^{2-}$ adduct was also validated in our precious study[17]. Similarly, an anodic shift in redox potential under CO_2 was observed in an aqueous electrolyte (Supplementary Fig. 1), suggesting that Id^{2-} is also capable of binding with CO_2 under typical CO_2RR conditions[21,22]. Density functional theory (DFT) calculation further supports that the complexation with Id^{2-} induces considerable restructuring of CO_2 molecules (Fig. 1c and Supplementary data 1). The CO_2 adduct adopts a bent configuration with a bond angle of 132.4° (O–C–O), and the two C–O bonds (bonds $a^{(\prime)}$and $b^{(\prime)}$) are elongated to 1.236–1.261 Å. The bent CO_2 and the redox-active oxygen center form a C–O bond (bonds $c^{(\prime)}$) with a length of ~ 1.486 Å. Given that the onset potential for CO_2 capture by Id (0.25 V vs. the reversible hydrogen electrode (RHE), Supplementary Fig. 1) is more positive than the equilibrium potential for CO_2RR-to-CO conversion (−0.10 V vs. RHE)[7], we hypothesize that the introduction of CO_2-binding Id to Ag catalysts could effectively active CO_2 by weakening its C=O bond strength during CO_2RR, thereby facilitating the subsequent reductive transformation.

To test our hypothesis, we ultrasonically mixed Id molecules with commercial Ag nanoparticles (AgNP, 20–40 nm in diameter) in isopropanol and spray-coated the resulting ink onto a carbon gas diffusion layer (GDL) to obtain the Id-modified Ag electrode (AgNP+Id). Scanning electron microscopy (SEM) images reveal that Id crystals are interspersed among agglomerated AgNP, and energy-dispersive X-ray spectroscopy (EDS) elemental mapping confirms the uniform distribution of both components across the electrode (Supplementary Fig. 2). The successful modification of the AgNP electrode with Id is also verified by X-ray photoelectron spectroscopy (XPS), which shows strong N 1*s* signals (Supplementary Fig. 3a). The Ag 3*d* XPS spectra indicate the chemical state of metallic Ag^0 for both bare AgNP and AgNP+Id (Supplementary Fig. 3b). These results suggest that Id modification by physical mixing has minimal impact on the morphology or electronic structure of AgNP.

The CO_2RR performance was accessed in a flow cell using 1 M potassium hydroxide (KOH) aqueous electrolyte. Compared to bare AgNP, the AgNP+Id electrode promotes CO selectivity by suppressing the competing HER to below 5%, especially at higher current densities (Supplementary Figs. 4 and 5). Specifically, AgNP+Id achieves a CO FE of 92% at a total current density (j_{total}) of $283\ mA\ cm^{-2}$, whereas CO FEs for AgNP rapidly drop to below 87% when j_{total} exceeds $173\ mA\ cm^{-2}$ (Fig. 1d). AgNP+Id also exhibits enhanced CO activity, as manifested by a ~ 70 mV decrease in overpotential at a j_{total} of $30\ mA\ cm^{-2}$ and a ~ 2.7-fold increase in CO partial current density (j_{CO}) at −0.57 V vs. RHE, compared to AgNP under the same conditions (Fig. 1e). Control experiments without AgNP indicate that improved reactivity upon the addition of Id shall be attributed to a synergistic effect between Id and AgNP since the Id-only sample predominantly generates hydrogen (H_2) with negligible CO production (Supplementary Fig. 6). The incorporation of Id molecules slightly decreases the electrochemically active surface area (ECSA), likely due to the blocking of the Ag surface by organic moieties (Supplementary Fig. 7 and Supplementary Table 1)[23]. Therefore, AgNP+Id delivers an even higher ECSA-normalized j_{CO} compared to bare AgNP (Supplementary Fig. 7d), excluding surface roughness as the contributor to the improved CO_2RR performance.

We conducted DFT calculations to gain a deeper understanding of the cooperativity between Id and Ag in CO_2 activation (Supplementary data 1). The results demonstrate that the configuration of adsorbed CO_2 at the Ag/Id interface resembles that of the $Id\text{-}2CO_2^{2-}$ adduct (Fig. 1f). The bent CO_2 molecule is stabilized through the redox-active

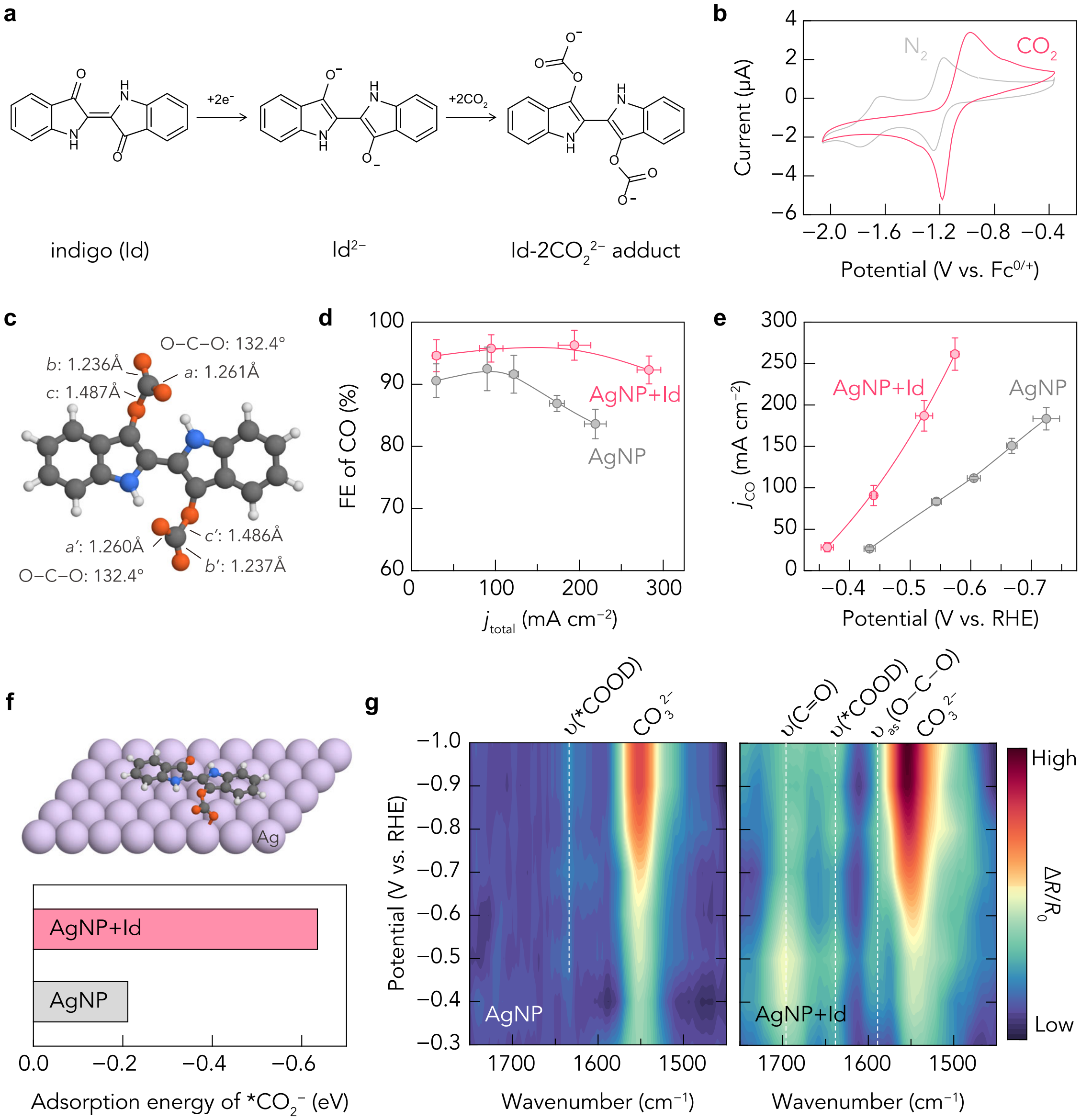

Fig. 1 | CO_2RR performance and mechanistic insight of AgNP+Id hybrid. **a** Reaction mechanism of redox-active Id for CO_2 capture. **b** CV of Id under N_2 and CO_2 atmospheres. The experiments were conducted by dissolving 2.5 mM Id in dimethyl sulfoxide (DMSO) with 0.1 M tetrabutylammonium hexafluorophosphate ($TBAPF_6$) at a scan rate of −20 mV s^{-1}. Ferrocene/ferrocenium ($Fc^{0/+}$) was used as an internal reference. Potentials are non-*iR* corrected. **c** DFT-optimized structure of Id-$2CO_2^{2-}$ adduct showing the bent CO_2 configuration at the redox-active oxygen center. The corresponding bond angles and lengths are listed next to the structure. The black, red, blue, and white spheres represent C, O, N, and H atoms, respectively. **d**, **e** Comparison of CO FE as a function of j_{total} (**d**), and j_{CO} as a function of potential (**e**) for AgNP and AgNP+Id. Potentials have been 100% *iR* corrected. The flow cell was operated with 1 M KOH (pH = 14.0 ± 0.2). Data are presented as mean ± s.d. Error bars represent s.d. from measurements of three independent electrodes. **f** Adsorption configuration of the $*CO_2^-$ intermediate at the Ag/Id interface and comparison of $*CO_2^-$ adsorption energies for AgNP and AgNP+Id. The black, red, blue, white, and purple spheres represent C, O, N, H, and Ag atoms, respectively. **g** Potential-dependent ATR-SEIRAS contour map for AgNP and AgNP/Id. $\Delta R/R_0 = (R - R_0)/R_0$, where R and R_0 are spectra collected at the sample potential and the open circuit potential, respectively. Source data are provided as a Source Data file.

oxygen center of reduced Id, with a $*CO_2^-$ adsorption energy of −0.635 eV. By contrast, $*CO_2^-$ exhibits much weaker adsorption energy of merely −0.211 eV on a pristine Ag surface, which is insufficient to initiate the CO_2 reduction pathway[24]. These preliminary findings indicate that the electro-activated Id moiety is a promising promoter to collectively stabilize CO_2 near the Ag surface, which is pivotal for boosting CO_2-to-CO conversion[24].

Building on the insights from DFT calculations, we then employed in situ attenuated total reflection surface-enhanced infrared absorbance spectroscopy (ATR-SEIRAS) to identify intermediate adsorption features during CO_2RR. Potential-dependent spectra were collected in CO_2-saturated D_2O with 0.1 M potassium phosphate as the electrolyte to minimize interference from adsorbed H_2O and (bi)carbonate ions (Fig. 1g and Supplementary Fig. 8). Both the AgNP and AgNP+Id samples show strong bands at ~1550 cm^{-1}, ascribed to the adsorbed CO_3^{2-} species[25,26]. The stronger intensity of this band for AgNP+Id could originate from the faster local proton consumption during CO_2RR. Bare AgNP displays a very weak band at ~1640 cm^{-1} (Fig. 1g), which corresponds to the C=O stretching of the *COOD intermediate (ν(*COOD))[27]. The redshift of this band relative to the reported wavenumber for *COOH might be due to the deuteration effect[25,28]. By contrast, we observe intensified ν(*COOD) bands emerging at lower overpotentials for AgNP+Id, implying accelerated kinetics of *COOD formation.

Importantly, additional bands arise exclusively for the Id-modified sample (Fig. 1g). We assign the band at ~1698 cm^{-1} to the carbonate C=O stretching of the Id-2CO_2^{2-} adduct (ν(C=O)), which closely matches the DFT-simulated vibration of 1675 cm^{-1} at the catalytic interface (Supplementary Fig. 9). The band intensity peaks at around −0.5 V vs. RHE and gradually decreases as the potential becomes more negative. Such a phenomenon reflects the progressive accumulation and conversion of activated $*CO_2^-$ species. In addition, the band at ~ 1590 cm^{-1} can likely be attributed to the asymmetric O−C−O stretching of $*CO_2^-$ evoked by the resonance structure of Id-2CO_2^{2-} (ν_{as}(O−C−O)), which merges with the CO_3^{2-} band at more cathodic potentials. It is noteworthy that the ν_{as}(O−C−O) band has been reported as weak or even undetectable on bare Ag, especially at low overpotentials[27]. Our observation of a strong ν_{as}(O−C−O) band implies the existence of an unconventional adsorption configuration of $*CO_2^-$ at the Ag/Id interface, such as partial Ag−O coordination[28,29], as also suggested by our DFT calculations (Fig. 1f). We also observe broader bands in the range of 1460–1530 cm^{-1}, though their precise assignments remain debatable. In some reports, these bands are associated with adsorbed CO_2 and/or protonated carbonate species[25,26]. Collectively, the in situ ATR-SEIRAS results support that the redox-active Id molecule can significantly facilitate CO_2 activation to form key intermediates at the Ag/Id interface, namely $*CO_2^-$ and *COOH, ultimately leading to promoted CO generation.

Optimizing CO_2 binding affinity on indigo derivatives

Our combined experimental and theoretical results confirmed the hypothesis that modifying Ag catalysts with CO_2-binding Id moieties can create reactive interfaces conducive to CO_2 activation and subsequent conversion to CO. Notably, the advantage of employing redox-active CO_2-binding organic molecules as promoters lies in the ability to leverage precise synthetic control to finetune their CO_2 affinities[18,20]. This enables the insightful interrogation of the correlations between molecular properties and catalytic performance and thus directs the optimization of intermediate adsorptions in the CO_2RR-to-CO pathway. Our previous studies demonstrated that introducing electron-withdrawing groups (EWGs, such as −Br and −COOH) to the structure of redox-active compounds weakens their interaction with CO_2 by reducing the electron density at the binding sites while introducing electron-donating groups (EDGs, such as $-OCH_3$ and $-OC_3H_7$) enhances CO_2 affinity[18]. Therefore, we synthesized a series of indigo derivatives with different substituent groups (see Supplementary Note 1 for synthesis details), including 5,5′,6,6′-tetramethoxylindigo (TMId), 5,5′-dipropoxyindigo (DPId), 6,6′-dibromoindigo (DBId), and indigo-6,6′-dicarboxylic acid (DCId), to investigate their impact on Ag-catalyzed CO_2RR.

CV curves of the synthesized indigo derivatives were examined in both aprotic and aqueous electrolytes to assess their CO_2 complexation behaviors (Supplementary Figs. 10 and 11). Similar to Id, all of these indigo derivatives exhibit chemical reactions with CO_2 upon electro-reduction in both environments, as evidenced by the positive shifts in redox potential under CO_2 compared to N_2 atmospheres. It is well-established that, in aprotic solvents, a linear scaling relationship exists between the reduction potential and the CO_2 affinity of redox-active CO_2-binding molecules[30]. Specifically, species with more anodic reduction potentials generally show weaker CO_2 affinities. Here, we find that the onset potentials for CO_2 capture in aprotic and aqueous electrolytes also display a strong linear correlation (Fig. 2a). This finding implies that molecular engineering remains effective in tuning the interaction strength between CO_2 and indigo derivatives in aqueous electrolytes, which is also supported by our DFT calculation (Supplementary Table 2). Thus, the CO_2 affinity of indigo derivatives gradually decreases across the series of TMId, DPId, Id, DBId, and DCId. Furthermore, it is reasonable to infer that this trend in CO_2 affinity can extend to the corresponding hybrid interface with Ag catalysts for CO_2RR, as corroborated by the AgNP+Id case discussed above.

The indigo derivatives were then used to modify AgNP catalysts following the same procedure as that used for AgNP+Id. Again, there are no apparent changes in the structure or chemical state of AgNP after modification (Supplementary Figs. 12–17). The as-prepared hybrids are denoted as AgNP+TMId, AgNP+DPId, AgNP+DBId, and AgNP+DCId, respectively. Introducing these indigo derivatives to AgNP drastically promotes CO_2RR compared to bare AgNP (Supplementary Figs. 18 and 19). All modified samples display similar enhancement in CO selectivity, achieving FEs of ~ 93% across the investigated current densities (Fig. 2b). Nevertheless, pronounced variations in j_{CO} with respect to overpotential can be observed. Using the CO activity of AgNP+Id as a benchmark, we found that indigos functionalized with EWGs (DBId and DCId) can further accelerate CO generation on Ag, while those functionalized with EDGs (TMId and DPId) demand higher overpotentials for CO_2-to-CO conversion (Fig. 2c). The best CO_2RR performance is achieved with DCId, whose CO_2 affinity is the weakest among the indigo derivatives. Specifically, AgNP+DCId attains a j_{CO} of 273 mA cm^{-2} at −0.54 V vs. RHE, which is ~ 2.6 times higher than that of AgNP+TMId (the derivative with the strongest CO_2 affinity) at a similar potential.

Intriguingly, we identified a linear relationship between the CO_2RR potential of the modified catalysts and the onset potential for CO_2 capture of various indigos (Fig. 2d). This indicates that the CO_2RR activity is strongly correlated with the varying $*CO_2^-$ adsorption energy at the catalytic interface. DFT calculations reveal that the $*CO_2^-$ adsorption energy at the Ag/DCId interface (−0.583 eV) falls between those of the Ag/Id interface (−0.635 eV) and the bare Ag surface (−0.211 eV, Supplementary Fig. 20). We postulate that, for an optimal CO_2RR performance, the CO_2-binding capabilities of molecular modifiers should be sufficiently strong to effectively stabilize the $*CO_2^-$ intermediate at the molecule/catalyst interface, yet not too strong to potentially slow down the subsequent hydrogenation and/or *CO desorption steps in the CO pathway[31]. To validate this hypothesis, we evaluated the CO_2RR performance of thioindigo-modified AgNP. Thioindigo has a much weaker interaction with CO_2 due to its electron-deficient nature[32], as evidenced by its nearly identical redox behavior under CO_2 and N_2 conditions in an aqueous electrolyte (Supplementary Fig. 21b and Supplementary Table 2). As a result, thioindigo shows no promotional effect on AgNP for CO_2-to-CO conversion (Supplementary Fig. 21). Plotting the CO_2RR potential against the onset potential for CO_2 capture over AgNP electrodes modified with various indigos affords a volcano-like trend (Supplementary Fig. 22), with AgNP+DCId exhibiting the most favorable $*CO_2^-$ adsorption energy toward CO formation in our case.

As a final note, no trends in CO_2RR activity were observed in relation to surface hydrophobicity or roughness across the different modified electrodes (Supplementary Figs. 23–25). The comparable ECSAs of these samples also suggest that the availability of Ag active sites is not substantially affected by the modification (Supplementary Table 1). These results rule out other possible factors as main contributors to the enhanced CO_2RR performance of AgNP modified with indigo derivatives.

Immobilizing CO_2-binding moieties via polymerization

Albeit being the most effective promoter, molecular DCId is susceptible to dissolution into the electrolyte during CO_2 electrolysis at relatively high current densities (Supplementary Fig. 26). To achieve a more stable molecular modification, we immobilized the redox-active CO_2-binding moieties into a macromolecular structure. As shown in Fig. 3a, we synthesized an indigo-based polymer (P-Id) by amidation between DCId and 2,2′-(ethylenedioxy)diethylamine (DODA, see Methods for synthesis details). Fourier-transform infrared (FTIR) spectroscopy of P-Id displays a vibration band associated with the

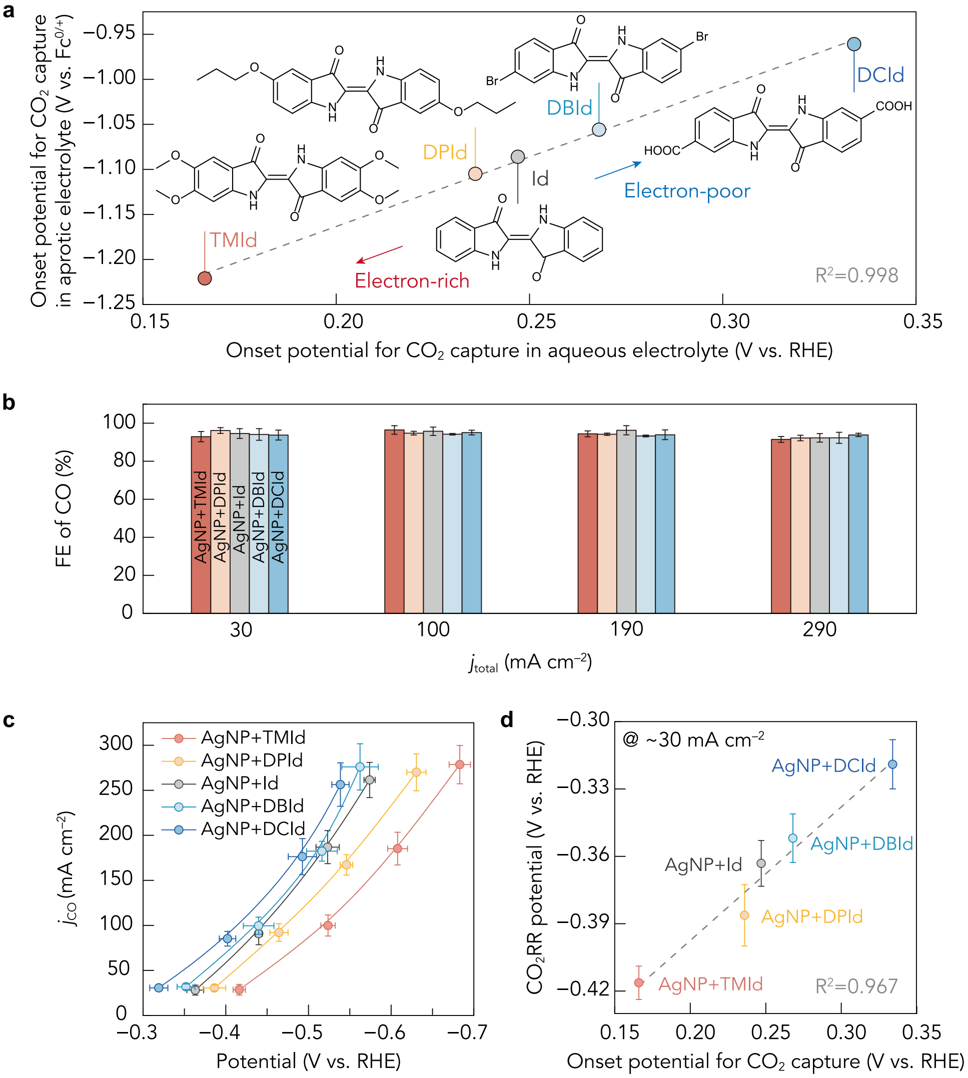

Fig. 2 | Electrochemical properties of indigo derivatives and their promotional effects on CO_2RR when modified on AgNP. a Linear relationship between the onset potentials for CO_2 capture in aprotic and aqueous electrolytes for indigos functionalized with EDGs or EWGs. **b**, **c** Comparison of CO FE at different j_{total} (**b**), and j_{CO} at different potentials (**c**) for AgNP modified with various indigos. **d** Correlation between the CO_2RR potential at a j_{total} of ~30 mA cm^{-2} for modified AgNP catalysts and the onset potential for CO_2 capture by various indigos. Potentials have been 100% *iR* corrected. The flow cell was operated with 1 M KOH (pH = 14.0 ± 0.2). Data are presented as mean ± s.d. Error bars represent s.d. from measurements of three independent electrodes. Source data are provided as a Source Data file.

amide C−N stretching at ~1540 cm^{-1}, accompanied by the disappearance of the C=O stretching band of carboxylic acid from the DCId precursor at ~1680 cm^{-1} (Fig. 3b). These findings indicate the successful amidation polymerization between the two precursors. The formation of the proposed P-Id structure is further verified by solid-state ^{13}C nuclear magnetic resonance (NMR) spectroscopy (Fig. 3c), where the observed peaks can be assigned to the different types of carbon marked in Fig. 3a.

It is important to note that the onset potential for CO_2 capture by P-Id closely matches that of DCId, confirming that the polymer structure retains the redox-active oxygen center without compromising its favorable CO_2 binding affinity (Supplementary Figs. 27 and 28). As anticipated, modifying AgNP with P-Id (AgNP+P-Id) by ultrasonic mixing results in substantially enhanced CO_2RR reactivity, with the CO FEs exceeding 90% across a wide range of j_{total} from 30 to 850 mA cm^{-2} (Fig. 3d and Supplementary Fig. 29). Particularly, AgNP+P-Id achieves a CO FE of 99% at a j_{total} of 100 mA cm^{-2}, slightly outperforming AgNP+DCId (95%) at a similar j_{total}. This additional improvement is likely due to further HER inhibition in the more hydrophobic microenvironment induced by P-Id (Supplementary Fig. 30). Given the comparable CO_2 affinity of the redox-active centers, AgNP+P-Id exhibits almost identical overpotentials to AgNP+DCId at relatively low current densities (Fig. 3e). However, AgNP+P-Id enables CO_2 electrolysis at much higher current densities (j_{CO} up to nearly 700 mA cm^{-2}), thanks to the suppressed solubility and enhanced robustness of P-Id, as substantiated by post-electrolytic characterizations (Supplementary Fig. 31).

Engineering Ag catalyst for enhanced utilization of Ag/indigo interfaces

To enhance the availability of catalytic interfaces, we sought to improve the dispersion and utilization of Ag active sites by incorporating highly porous carbon black as the catalyst support (Supplementary Fig. 32). Carbon supports typically offer a better conductive network, mitigate nanoparticle agglomeration, and increase mass activity by reducing catalyst loading[33,34]. Therefore, we prepared a carbon-supported Ag catalyst with abundant surface defects (D-Ag/C) via in situ electrodeposition (see Methods for synthesis details).

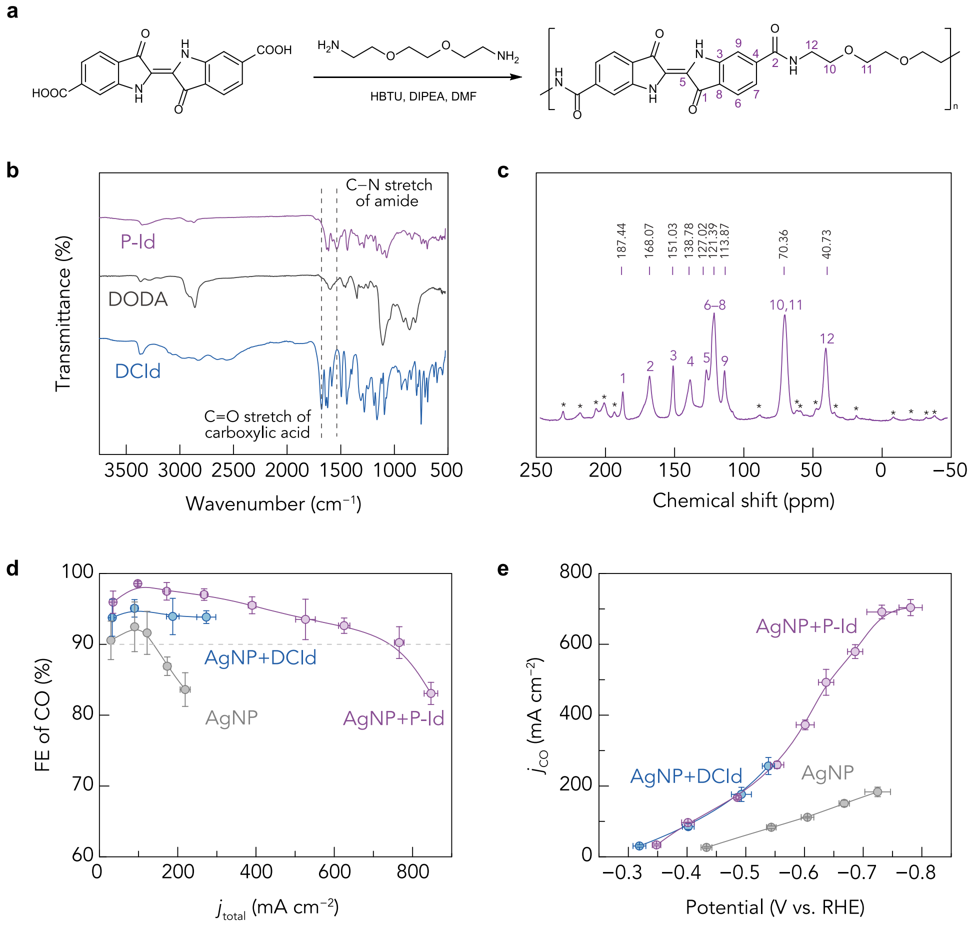

Fig. 3 | Synthesis and characterization of P-Id for a stable modification on AgNP. a Synthesis of P-Id. HBTU: 2-(1*H*-benzotriazol-1-yl)−1,1,3,3-tetramethyluronium hexafluorophosphate; DIPEA: *N*,*N*-diisopropylethylamine; DMF: *N*,*N*-dimethylformamide. **b** FTIR spectra of DCId, DODA, and P-Id. **c** Solid-state ^{13}C NMR spectrum of P-Id. The peaks are assigned to the corresponding carbons labeled in (**a**). Asteroids denote spinning sidebands. **d**, **e** Comparison of CO FE as a function of j_{total} (**d**), and j_{CO} as a function of potential (**e**) for AgNP, AgNP+DCId, and AgNP+P-Id. Potentials have been 100% *iR* corrected. The flow cell was operated with 1 M KOH (pH = 14.0 ± 0.2). Data are presented as mean ± s.d. Error bars represent s.d. from measurements of three independent electrodes. Source data are provided as a Source Data file.

The Ag loading on the GDL was 6 µg cm^{-2} (equivalent to 2 wt% on carbon black) measured by the inductively coupled plasma optical emission spectrometry (ICP-OES). High-angle annular dark-field scanning transmission electron microscopy (HAADF-STEM) and corresponding STEM-EDS mapping show that the Ag particles obtained via in situ electrodeposition have an average diameter of ~28 nm and are primarily isolated and well dispersed on the carbon matrix (Fig. 4a and Supplementary Fig. 33). High-resolution transmission electron microscopy (HRTEM) images indicate the presence of planar defects on the Ag surface (Fig. 4b and Supplementary Fig. 34), which can provide uncoordinated sites to potentially enhance CO_2 conversion[35,36]. X-ray absorption spectroscopy (XAS) was applied to probe the electronic state and coordination structure of the D-Ag/C catalyst. The normalized X-ray absorption near-edge structure (XANES) spectra at the Ag K-edge confirm the metallic Ag nature of D-Ag/C (Fig. 4c), consistent with the XPS result (Supplementary Fig. 35). The Ag K-edge extended X-ray absorption fine structure (EXAFS) spectra (*R*-space) show the lowest intensity of peaks between 1.5 and 3.3 Å, corresponding to the first nearest neighboring Ag–Ag bond for D-Ag/C, in comparison to Ag foil and commercial AgNP (Fig. 4d). Corresponding fitting analysis indicates that the coordination numbers (*CN*s) of Ag decrease in the order: Ag foil (12) > commercial AgNP (10.8 ± 0.4) > D-Ag/C (8.0 ± 0.6) (Fig. 4e, Supplementary Fig. 36 and Supplementary Table 3). The slight *CN* diminution in AgNP relative to Ag foil is ascribed to the small particle size, while the further diminution in *CN* for D-Ag/C shall be mainly driven by the existence of abundant planar defects[37].

We subsequently benchmarked the CO_2RR performance of D-Ag/C in a flow cell. D-Ag/C possesses superior CO_2RR reactivity compared to carbon-supported AgNP (AgNP/C) with the same Ag loading of 6 µg cm^{-2} (Supplementary Fig. 37). Furthermore, D-Ag/C achieves a maximum CO FE of 94% and a j_{CO} of 279 mA cm^{-2} at −0.73 V vs. RHE (Fig. 5a and b). These values are ~1.1- and ~1.5-fold higher, respectively than those of commercial AgNP with a much higher Ag loading of 0.4 mg cm^{-2} at the same potential (Supplementary Fig. 37). The combination of the carbon support and the in situ electrodeposition method effectively prevents the aggregation of defective Ag particles and increases the density of highly active sites participating in CO_2RR, leading to a significant enhancement in CO production for D-Ag/C.

The highly dispersed D-Ag/C catalyst provides exciting opportunities for creating rich catalytic interfaces when modified with P-Id. Indeed, introducing P-Id to D-Ag/C (D-Ag/C+P-Id) increases the j_{CO} to 818 mA cm^{-2} at −0.73 V vs. RHE, nearly tripling the performance of bare D-Ag/C at the same potential, meanwhile maintaining a high CO FE of 93% (Fig. 5a, b and Supplementary Fig. 38). Analogous to the AgNP+P-Id case, P-Id modification drastically extends the CO_2-to-CO conversion across a wider current density range (Fig. 5a). The FEs for CO exceed 95% at a j_{total} ranging from 188 to 780 mA cm^{-2}.

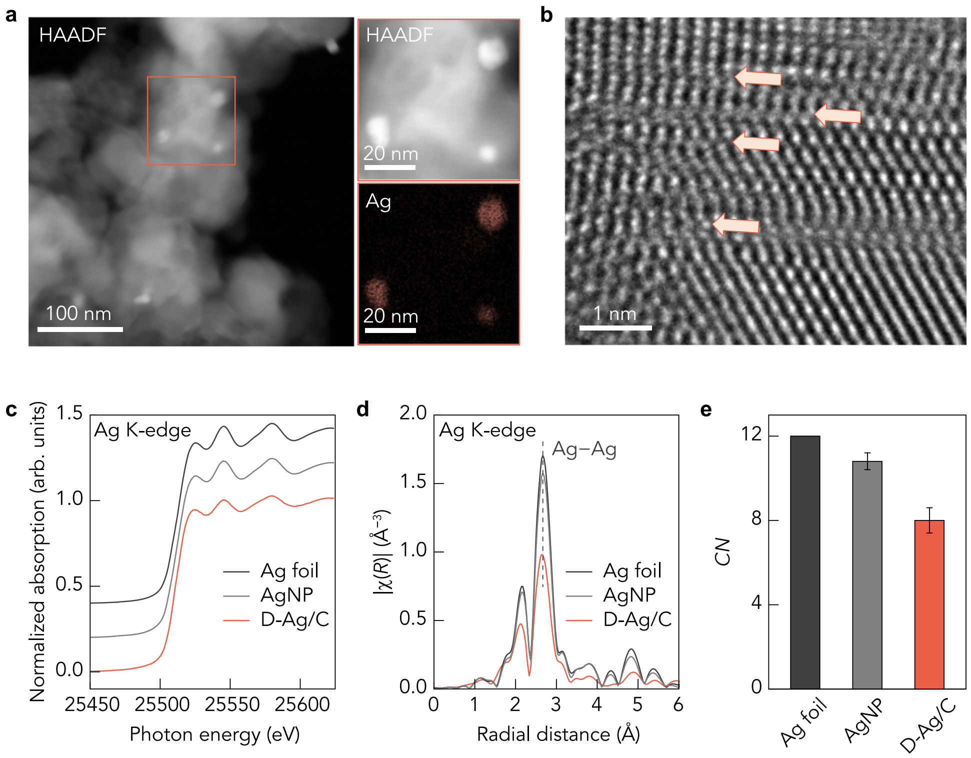

Fig. 4 | Morphological and structural characterizations of D-Ag/C catalyst. **a** HAADF-STEM and STEM-EDS mapping of the D-Ag/C catalyst showing isolated Ag particles on carbon support. **b** HRTEM image of the D-Ag/C catalyst showing abundant planar defects (denoted by arrows). **c**, **d** XANES data (**c**) and Fourier transform magnitudes of the k^2-weighted EXAFS spectra (**d**) at the Ag K-edge of AgNP and D-Ag/C. The spectra of Ag foil were shown as a reference. **e** The Ag–Ag coordination numbers obtained by theoretical fits to the EXAFS data. Source data are provided as a Source Data file.

Remarkably, the FE for CO remains at 91% when the j_{total} is ramped up to 1.17 A cm^{-2} at −0.80 V vs. RHE, ranking among the highest performances reported to date (Fig. 5c). The low Ag loading gives rise to a high mass activity of 174 A mg$^{-1}_{\mathrm{Ag}}$ for CO production at −0.80 V vs. RHE (Fig. 5c), which is nearly two orders of magnitude higher than previously reported AgNP catalysts and even outperforms state-of-the-art single-atom catalysts (SACs) for the CO_2RR to CO (Fig. 5d and Supplementary Table 4). Note that H_2 is the only product from electrolysis under an argon atmosphere, which confirms that the carbon source of CO evolution originates from the CO_2 feedstock (Supplementary Fig. 39). Such a collective strategy could potentially pave the way for large-scale, cost-effective, and sustainable CO_2-to-CO conversion (see Supplementary Note 2 for more discussions).

To improve the full-cell energy efficiency (EE), the D-Ag/C+P-Id catalyst was integrated into a zero-gap membrane electrode assembly (MEA) cell. The catalyst-coated membrane (CCM) method was utilized on the cathode and paired with a highly efficient Ni foam-supported Ni-Fe oxide as the anode to minimize voltage loss (Supplementary Fig. 40)[38–40]. The MEA cell, operated at 50 °C with 0.2 M cesium hydroxide (CsOH) as the anolyte, yields steady CO selectivity across the investigated current density range of 0.10–1.20 A cm^{-2} at cell voltages between 2.34 and 3.89 V (Fig. 6a). A peak CO FE of 94% with a j_{CO} of 375 mA cm^{-2} is achieved at a cell voltage of 2.89 V, corresponding to an EE of 43% (Fig. 6b). The MEA cell also exhibits marginal decay in CO production performance over at least 20 hours at a j_{total} of 400 mA cm^{-2} (Fig. 6c). Post-reaction characterizations demonstrate the promising durability of both the D-Ag/C and P-Id components (Supplementary Figs. 41 and 42).

Discussion

In summary, using redox-active indigo molecules as a model system, we demonstrate that decorating Ag-based catalysts with electro-activated CO_2-binding organics creates synergistic interfaces that significantly enhance both the selectivity and activity of CO_2-to-CO conversion. The dynamic complexation interactions between these organic promoters and CO_2 readily activate CO_2 molecules and effectively enrich the $^*CO_2^-$ and *COOH intermediates at the nearby Ag catalytic sites. Importantly, by precisely tuning the CO_2 binding affinities of indigo derivatives via molecular engineering, we unravel a critical volcano-like relationship between the $^*CO_2^-$ adsorption energy induced by organic modifiers and their promotional effect on CO_2RR. This mechanistic insight culminates in the development of a hybrid catalyst that couples polymerized indigo moieties with the optimal CO_2 affinity and highly dispersed, defect-rich Ag particles, achieving impressive CO_2RR performance at ampere-level current densities. Furthermore, we anticipate that this redox-active molecular platform can be extended to benefit CO_2 electrolysis to high-value multi-carbon products when incorporated into copper-based catalysts. Our work opens new avenues for the rational design of highly efficient, molecularly tailored catalysts. Moreover, the integration of CO_2-binding species with CO_2RR catalysts could potentially enable a desirable reactive carbon capture scheme where CO_2 from dilute sources is directly converted into chemicals and fuels without prior concentration, offering advantages in process intensification and energy efficiency.

Methods

Chemicals and materials

Silver nanopowder (20–40 nm, 99.9%) and silver nitrate ($AgNO_3$, 99.9%) were obtained from Thermo Scientific. Indigo powder (97.0%) was purchased from TCI America. Chemicals for polymerization, including HBTU (99.0%), DIPEA (99.5%), DODA (98.0%), and DMF (99.9%), were purchased from Sigma Aldrich. All chemicals are used as received without purification.

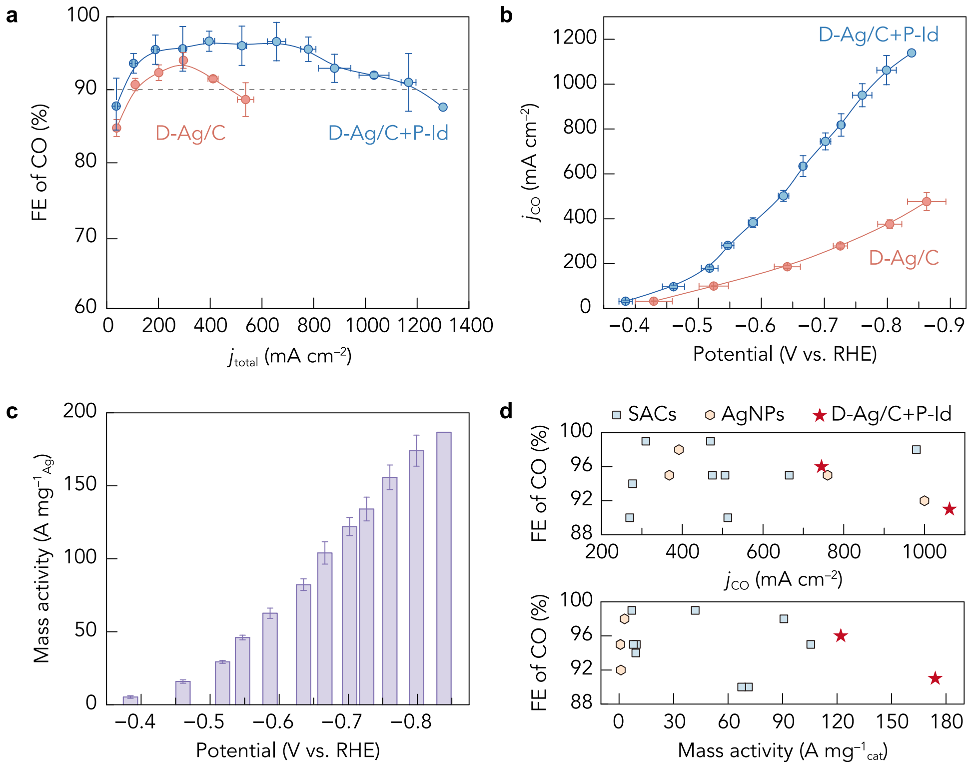

Fig. 5 | CO_2RR performance of D-Ag/C and D-Ag/C+P-Id catalysts. **a**, **b** Comparison of CO FE as a function of j_{total} (**a**), and j_{CO} as a function of potential (**b**) for the D-Ag/C and D-Ag/C + P-Id catalysts. **c** Ag mass activity toward CO product at different potentials for the D-Ag/C + P-Id catalyst. Potentials have been 100% *iR* corrected. The flow cell was operated with 1 M KOH (pH =14.0 ± 0.2). Data are presented as mean ± s.d. Error bars represent s.d. from measurements of three independent electrodes. **d** Performance comparison of D-Ag/C+P-Id with reported electrocatalysts for CO_2RR to CO in the gas diffusion electrode (GDE)-based electrolyzer. Details are given in Supplementary Table 4. Source data are provided as a Source Data file.

Organic synthesis

Synthesis procedures for indigo derivatives are provided in Supplementary Note 1. P-Id was prepared via amidation polymerization. Specifically, to a mixture of DCId (0.7 g, 2 mmol) and HBTU (1.64 g, 2.16 mmol) in anhydrous DMF (30 ml) was added DIPEA (2.09 ml, 12 mmol) dropwise. The mixture was stirred for 30 mins before DODA (2 mmol, 292 µl) was added. The reaction was stirred for another 24 hours at room temperature (20 °C) and poured into a saturated $NaHCO_3$ aqueous solution (200 ml). The precipitate was collected by filtration, washed sequentially with saturated $NaHCO_3$ (aq), water, 0.2 M HCl (aq), cold methanol, and dichloromethane, and dried in vacuo to give a dark blue solid (784 mg, 85% yield).

D-Ag/C catalyst synthesis

The D-Ag/C catalyst was synthesized using the in situ electrodeposition method. Vulcan XC-72 carbon black suspension (10 mg ml^{-1}) was added to $AgNO_3$ aqueous solution (0.33 mg ml^{-1}) and sonicated in an ice bath for 2 h to allow the uniform dispersion of Ag^+ on the carbon black support. The resulting slurry was added to isopropanol with 5 wt% Nafion solution to obtain the catalyst ink, which was then spray-coated on GDL (Sigracet 39BB) until reaching a total mass loading of 0.3 mg cm^{-2}. The D-Ag/C catalyst was formed in situ by reducing the as-prepared GDE at 30 mA cm^{-2} for 15 min in the flow cell supplied with CO_2 gas and 1 M KOH. The final Ag loading on the GDE was ~ 6 µg cm^{-2} measured by ICP-OES.

Material characterizations

FTIR spectra were collected on a Thermo Fischer Nicolet iS5 spectrometer. Solid-state ^{13}C NMR spectrum was obtained from a Bruker Ascend 500 MHz Solids at a spin rate of 10000 Hz. Liquid ^{1}H NMR spectra were recorded on a Bruker Avance 400 MHz with solvent residue peak as the internal reference. SEM images were collected on a Helios G5-focused ion beam SEM. XPS measurements were carried out using a PHI Quantera XPS equipped with the Al Kα radiation source. HAADF-STEM, STEM-EDS elemental mapping, and HRTEM were collected from a FEI Titan Themis^3 S/TEM. XAS measurements were performed on the Beamline 7-BM of the National Synchrotron Light Source II (NSLS II) at Brookhaven National Laboratory. The Athena and Artemis software in the Demeter package was applied for data processing and analysis[41]. The theoretical EXAFS signal was fitted to the experimental EXAFS data in *R*-space by Fourier transforming both the theoretical and experimental data.

Electrochemical measurements

CV measurements were carried out on a BioLogic VSP potentiostat (BioLogic Science Instruments). Glassy carbon (3 mm in diameter) was used as the working electrode, and Pt wire was used as the counter electrode. For measurements conducted in aprotic electrolytes, Ag wire was used as a pseudo-reference electrode, and ferrocene was used as an internal reference. The organic compound (2.5 mM) was dissolved in DMSO with 100 mM $TBAPF_6$ as the supporting salt. For measurements conducted in aqueous electrolytes, Ag/AgCl (3 M KCl) was used as the reference electrode. The reference electrode was calibrated using a standard hydrogen electrode before measurements. The compound was mixed with Vulcan XC-72 (mass ratio of 1:1) in isopropanol and drop-casted onto the glassy carbon electrode. The pH of the electrolyte (1 M $KHCO_3$ saturated with either N_2 or CO_2) was measured by a pH meter (SevenCompact). The potential was converted to the RHE scale using $E_{RHE} = E_{Ag/AgCl} + 0.209\,V + 0.0591 \times pH$. CV curves were collected at the scan rate of −20 and −10 mV s^{-1} for the aprotic and aqueous conditions, respectively.

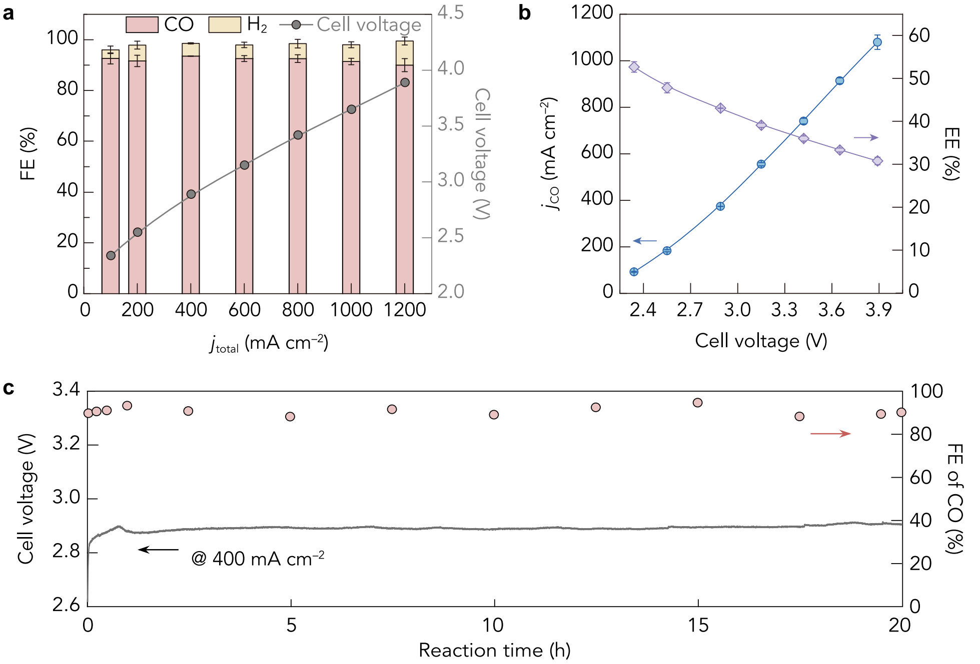

Fig. 6 | CO_2RR performance of D-Ag/C+P-Id catalyst in MEA cell. a FE and cell voltage at different j_{total}. **b** j_{CO} and EE for CO at different cell voltages without *iR* compensation. Data are presented as mean ± s.d. Error bars represent s.d. from three independent measurements. **c** CO_2RR stability at a j_{total} of 400 mA cm^{-2} when operating the MEA cell at 50 °C using 0.2 M CsOH (pH = 13.2 ± 0.1) as the anolyte.

Electrocatalytic CO_2RR measurements

CO_2RR performances were evaluated in a flow cell at 20 °C with 1 M KOH (pH = 14.0 ± 0.2) as the electrolyte. The fresh electrolyte was prepared using a volumetric flask before the testing. For the GDE fabrication, AgNP or AgNP mixed with organic species of interest were dispersed in isopropanol with 5 wt% Nafion. The concentration of AgNP was 5 mg ml^{-1}. The molar ratio of small molecules to AgNP was kept at 10%. The P-Id content was 50 wt% relative to AgNP. After sonication for 2 h, the ink was spray-coated onto the GDL. The Ag loading was controlled to be ~ 0.4 mg cm^{-2} for all samples. The GDE cathode and Ni foam anode were separated by an anion exchange membrane (AEM; Sustainion X37-50, 50 µm, 3 × 3 cm^2). AEM was submerged into 1 M KOH for 12 h and rinsed with deionized water before assembling into the cell. A multichannel peristaltic pump (Ismatec) was applied to feed the electrolyte (30 ml) at 1 ml min^{-1} and 2 ml min^{-1} to the cathodic and anodic compartments, respectively. A mass flow controller (Alicat Scientific) was employed to control the CO_2 gas flow rate at 50 standard cubic centimeters per minute (sccm) to the cathode. The CO_2RR experiments were operated in the chronoamperometry mode under ambient conditions on a BioLogic VSP potentiostat. When the current density exceeded 1 A cm^{-2}, a d.c. power supply (B&K Precision) was used instead of the potentiostat. The cathodic potential was determined relative to the Ag/AgCl (3 M) reference electrode and converted to the RHE scale accordingly. Because of the rapid dynamic evolutions of local environments, the resistance (R) between the cathode and reference electrode was immediately measured using potentiostatic electrochemical impedance spectroscopy (PEIS) after each electrolysis, and then the ohmic drop (*iR*) was 100% manually compensated to each potential. The R was around 3.3 ± 0.3 Ω for an electrode area of 1 cm^2. Non-*iR* corrected data were provided in Supplementary Table 5.

In the MEA setup, a more robust AEM (PiperION, 40 µm, 3 × 3 cm^2)[42] was used for the CCM fabrication. In brief, the catalyst was airbrushed onto the AEM directly, and combined with a highly hydrophobic GDL (Tory 090) to form the cathode[38]. The anode, Ni-Fe oxide, was prepared using a reported electrodeposition method on Ni foam[39]. The MEA cell was operated at 50 °C with 0.2 M CsOH (pH = 13.2 ± 0.1) as the anolyte to mitigate salt precipitation and the consequent electrode flooding[43]. The catalyst, membrane, and cell setup were initially activated at 30 mA cm^{-2} for 2 h before starting the performance measurements. The cell voltage was recorded without the *iR* correction.

During CO_2 electrolysis, an online gas chromatograph (GC, Shimadzu GC-2014) equipped with a thermal conductivity detector was employed to monitor the gas products. The FEs of gas products were calculated as follows:

$$FE(\%) = \frac{zFxV}{j_{total}} \times 100\%$$

where *z* is the number of electrons transferred to form a target product; *F* is the Faraday constant; *x* is the molar fraction of a target product determined by GC; *V* is the molar flow rate of effluent gas measured using a digital flow meter (Omega); and j_{total} is the total current density.

The EEs of CO were calculated as follows:

$$EE(\%) = \frac{1.23 - E^0_{CO}}{E_{cell}} \times FE_{CO}$$

where E^0_{CO} is the equilibrium potential for CO_2RR to CO (− 0.10 V vs. RHE)[7]; E_{cell} is the applied cell voltage; and FE_{CO} is the FE for CO.

In situ ATR-SEIRAS measurements

The ATR-SEIRAS setup was assembled according to prior works[44,45]. The catalyst ink was drop-casted onto a silicon ATR wafer with a thermal-evaporated Ag film (30 nm). The catalyst loading was controlled to be 0.4 mg cm^{-2}. Graphite rod and Ag/AgCl (3 M KCl) were used as the counter and reference electrodes, respectively. The SEIRAS spectra were recorded using a Thermo Fischer Nicolet iS50 spectrometer equipped with an N_2 cooled HgCdTe (MCT) detector and a Veemax III IR attachment from PIKE. The spectrometer was operated at a scan rate of 30 kHz. Spectra were acquired with a spectral resolution of 4 cm^{-1}, and 16 interferograms were coadded for each spectrum. During in situ measurements, the electrolyte (0.1 M potassium phosphate in D_2O) was continuously sparged with CO_2. CO_2 electrolysis was carried out at potentials ranging from −0.1 to −1.0 V vs. RHE. The spectrum collected at open circuit potential was used as the reference.

DFT calculations

DFT calculations were performed using the Vienna Ab initio Simulation Package (VASP)[46]. The Perdew-Burke-Ernzerhof (PBE) functional[47] was applied, with a plane wave energy cutoff of 400 eV. Van der Waals interactions were accounted for using the DFT-D3 dispersion correction[48]. A constant potential of −0.3 V vs. RHE was used in the simulations, and the pH was set to 14, reflecting the alkaline conditions of the electrolyte. Silver relaxation was modeled using a (6 × 6 × 6) supercell with a 15 Å vacuum gap, and the Gamma point was employed for k-point sampling. The adsorption of CO_2 and indigo on the Ag(111) surface was studied using the constant-potential model (CPM)[49] with a VASPsol patch to consider the implicit solvation[50,51]. The adsorption of two CO_2 molecules on the indigo and its derivatives was calculated with two extra electrons. Considering the increased complexity of the derivative molecules and the need for a much larger Ag surface, we calculated the adsorption on isolated molecules for qualitative analysis (Supplementary Table 2).

Data availability

All the data that support the findings of this study are available in the main text and the Supplementary Information. Data are also available from the corresponding author upon request. Source data are provided in this paper.

References

1. Birdja, Y. Y. et al. Advances and challenges in understanding the electrocatalytic conversion of carbon dioxide to fuels. *Nat. Energy* **4**, 732–745 (2019).
2. Jin, S., Hao, Z., Zhang, K., Yan, Z. & Chen, J. Advances and challenges for the electrochemical reduction of CO_2 to CO: from fundamentals to industrialization. *Angew. Chem. Int. Ed.* **60**, 20627–20648 (2021).
3. De Luna, P. et al. What would it take for renewably powered electrosynthesis to displace petrochemical processes? *Science* **364**, eaav3506 (2019).
4. Shin, H., Hansen, K. U. & Jiao, F. Techno-economic assessment of low-temperature carbon dioxide electrolysis. *Nat. Sustain.* **4**, 911–919 (2021).
5. Yu, S. & Jain, P. K. Plasmonic photosynthesis of C_1–C_3 hydrocarbons from carbon dioxide assisted by an ionic liquid. *Nat. Commun.* **10**, 2022 (2019).
6. Singh, M. R., Goodpaster, J. D., Weber, A. Z., Head-Gordon, M. & Bell, A. T. Mechanistic insights into electrochemical reduction of CO_2 over Ag using density functional theory and transport models. *Proc. Natl. Acad. Sci. USA* **114**, E8812–E8821 (2017).
7. Kuhl, K. P. et al. Electrocatalytic conversion of carbon dioxide to methane and methanol on transition metal surfaces. *J. Am. Chem. Soc.* **136**, 14107–14113 (2014).
8. Zhao, S., Jin, R. & Jin, R. Opportunities and challenges in CO_2 reduction by gold- and silver-based electrocatalysts: from bulk metals to nanoparticles and atomically precise nanoclusters. *ACS Energy Lett.* **3**, 452–462 (2018).
9. Nam, D.-H. et al. Molecular enhancement of heterogeneous CO_2 reduction. *Nat. Mater.* **19**, 266–276 (2020).
10. Zhang, J. et al. Molecular tuning for electrochemical CO_2 reduction. *Joule* **7**, 1700–1744 (2023).
11. Sanz-Pérez, E. S., Murdock, C. R., Didas, S. A. & Jones, C. W. Direct capture of CO_2 from ambient air. *Chem. Rev.* **116**, 11840–11876 (2016).
12. Zeng, S. et al. Ionic-liquid-based CO_2 capture systems: structure, interaction and process. *Chem. Rev.* **117**, 9625–9673 (2017).
13. Sun, J. W. et al. Direct oxygen-containing simulated flue gas electrolysis over amine-confined Ag catalyst in a flow cell. *Chem. Catal.* **4**, 100923 (2024).
14. Abdinejad, M. et al. CO_2 electrolysis via surface-engineering electrografted pyridines on silver catalysts. *ACS Catal.* **12**, 7862–7876 (2022).
15. Dongare, S. et al. A bifunctional ionic liquid for capture and electrochemical conversion of CO_2 to CO over silver. *ACS Catal.* **13**, 7812–7821 (2023).
16. Campos, K. R. Direct sp^3 C–H bond activation adjacent to nitrogen in heterocycles. *Chem. Soc. Rev.* **36**, 1069–1084 (2007).
17. Jayarapu, K. N. et al. Indigo as a low-cost redox-active sorbent for electrochemically mediated carbon capture. *Adv. Funct. Mater.* **34**, 2402355 (2024).
18. Li, X., Zhao, X., Liu, Y., Hatton, T. A. & Liu, Y. Redox-tunable Lewis bases for electrochemical carbon dioxide capture. *Nat. Energy* **7**, 1065–1075 (2022).
19. Li, X. et al. Redox-tunable isoindigos for electrochemically mediated carbon capture. *Nat. Commun.* **15**, 1175 (2024).
20. Li, X., Mathur, A., Liu, A. & Liu, Y. Electrifying carbon capture by developing nanomaterials at the interface of molecular and process engineering. *Acc. Chem. Res.* **56**, 2763–2775 (2023).
21. Liu, Y., Ye, H.-Z., Diederichsen, K. M., Van Voorhis, T. & Hatton, T. A. Electrochemically mediated carbon dioxide separation with quinone chemistry in salt-concentrated aqueous media. *Nat. Commun.* **11**, 2278 (2020).
22. Jing, Y. et al. Electrochemically induced CO_2 capture enabled by aqueous quinone flow chemistry. *ACS Energy Lett.* **9**, 3526–3535 (2024).
23. Chen, B. et al. Molecular enhancement of direct electrolysis of dilute CO_2. *ACS Energy Lett.* **9**, 911–918 (2024).
24. Monteiro, M. C. O. et al. Absence of CO_2 electroreduction on copper, gold and silver electrodes without metal cations in solution. *Nat. Catal.* **4**, 654–662 (2021).
25. Zhang, Z.-M. et al. Probing electrolyte effects on cation-enhanced CO_2 reduction on copper in acidic media. *Nat. Catal.* **7**, 807–817 (2024).
26. Moradzaman, M. & Mul, G. Infrared analysis of interfacial phenomena during electrochemical reduction of CO_2 over polycrystalline copper electrodes. *ACS Catal.* **10**, 8049–8057 (2020).
27. Firet, N. J. & Smith, W. A. Probing the reaction mechanism of CO_2 electroreduction over Ag films via operando infrared spectroscopy. *ACS Catal.* **7**, 606–612 (2017).
28. Delmo, E. P. et al. In situ infrared spectroscopic evidence of enhanced electrochemical CO_2 reduction and C–C coupling on oxide-derived copper. *J. Am. Chem. Soc.* **146**, 1935–1945 (2024).
29. Chernyshova, I. V., Somasundaran, P. & Ponnurangam, S. On the origin of the elusive first intermediate of CO2 electroreduction. *Proc. Natl. Acad. Sci. USA* **115**, E9261–E9270 (2018).
30. Barlow, J. M. & Yang, J. Y. Oxygen-stable electrochemical CO_2 capture and concentration with quinones using alcohol additives. *J. Am. Chem. Soc.* **144**, 14161–14169 (2022).
31. Hansen, H. A., Varley, J. B., Peterson, A. A. & Nørskov, J. K. Understanding trends in the electrocatalytic activity of metals and enzymes for CO_2 reduction to CO. *J. Phys. Chem. Lett.* **4**, 388–392 (2013).

32. Bauer, H., Kowski, K., Kuhn, H., Lüttke, W. & Rademacher, P. Photoelectron spectra and electronic structures of some indigo dyes. *J. Mol. Struct.* **445**, 277–286 (1998).
33. Ma, S. et al. Carbon nanotube containing Ag catalyst layers for efficient and selective reduction of carbon dioxide. *J. Mater. Chem. A* **4**, 8573–8578 (2016).
34. Sun, H. et al. Promoting ethylene production over a wide potential window on Cu crystallites induced and stabilized via current shock and charge delocalization. *Nat. Commun.* **12**, 6823 (2021).
35. Wu, X. et al. Fast operando spectroscopy tracking in situ generation of rich defects in silver nanocrystals for highly selective electrochemical CO_2 reduction. *Nat. Commun.* **12**, 660 (2021).
36. Mariano, R. G., McKelvey, K., White, H. S. & Kanan, M. W. Selective increase in CO_2 electroreduction activity at grain-boundary surface terminations. *Science* **358**, 1187–1192 (2017).
37. She, X. et al. Pure-water-fed, electrocatalytic CO_2 reduction to ethylene beyond 1,000 h stability at 10 A. *Nat. Energy* **9**, 81–91 (2024).
38. Rios Amador, I. et al. Protocol for assembling and operating bipolar membrane water electrolyzers. *STAR Protoc.* **4**, 102606 (2023).
39. Lu, X. & Zhao, C. Electrodeposition of hierarchically structured three-dimensional nickel–iron electrodes for efficient oxygen evolution at high current densities. *Nat. Commun.* **6**, 6616 (2015).
40. Hansen, K. U., Cherniack, L. H. & Jiao, F. Voltage loss diagnosis in CO_2 electrolyzers using five-electrode technique. *ACS Energy Lett.* **7**, 4504–4511 (2022).
41. Ravel, B. & Newville, M. ATHENA, ARTEMIS, HEPHAESTUS: data analysis for X-ray absorption spectroscopy using IFEFFIT. *J. Synchrotron Radiat.* **12**, 537–541 (2005).
42. Endrődi, B. et al. High carbonate ion conductance of a robust PiperION membrane allows industrial current density and conversion in a zero-gap carbon dioxide electrolyzer cell. *Energy Environ. Sci.* **13**, 4098–4105 (2020).
43. Cofell, E. R., Nwabara, U. O., Bhargava, S. S., Henckel, D. E. & Kenis, P. J. A. Investigation of electrolyte-dependent carbonate formation on gas diffusion electrodes for CO_2 electrolysis. *ACS Appl. Mater. Interfaces* **13**, 15132–15142 (2021).
44. Gerke, C. S. et al. Electrochemical C–N bond formation within boron imidazolate cages featuring single copper sites. *J. Am. Chem. Soc.* **145**, 26144–26151 (2023).
45. Gerke, C. S., Klenk, M., Zapol, P. & Thoi, V. S. Pulsed-potential electrolysis enhances electrochemical C–N coupling by reorienting interfacial ions. *ACS Catal.* **13**, 14540–14547 (2023).
46. Kresse, G. & Furthmüller, J. Efficient iterative schemes for ab initio total-energy calculations using a plane-wave basis set. *Phys. Rev. B* **54**, 11169–11186 (1996).
47. Perdew, J. P., Burke, K. & Ernzerhof, M. Generalized gradient approximation made simple. *Phys. Rev. Lett.* **77**, 3865–3868 (1996).
48. Grimme, S., Antony, J., Ehrlich, S. & Krieg, H. A consistent and accurate ab initio parametrization of density functional dispersion correction (DFT-D) for the 94 elements H-Pu. *J. Chem. Phys.* **132**, 154104 (2010).
49. Zhao, X. & Liu, Y. Origin of selective production of hydrogen peroxide by electrochemical oxygen reduction. *J. Am. Chem. Soc.* **143**, 9423–9428 (2021).
50. Mathew, K., Sundararaman, R., Letchworth-Weaver, K., Arias, T. A. & Hennig, R. G. Implicit solvation model for density-functional study of nanocrystal surfaces and reaction pathways. *J. Chem. Phys.* **140**, 084106 (2014).
51. Mathew, K., Kolluru, V. S. C., Mula, S., Steinmann, S. N. & Hennig, R. G. Implicit self-consistent electrolyte model in plane-wave density-functional theory. *J. Chem. Phys.* **151**, 234101 (2019).

Acknowledgements

We acknowledge financial support from the Johns Hopkins University, the David and Lucile Packard Foundation, the Arnold and Mabel Beckman Foundation, and the National Science Foundation (NSF grant number 2237096). This work was partially performed at the Materials Characterization and Processing Center in the Whiting School of Engineering at Johns Hopkins University. Yayuan Liu and V.S.T. are grateful for the support of the Ralph S. O'Connor Sustainable Energy Institute (ROSEI). R.W. and Yuanyue Liu acknowledge the support by Welch Foundation (F-1959), and the computational resources provided by ACCESS and NREL. C.S.G and V.S.T. acknowledge the U.S. Department of Energy (DOE), Office of Science, Office of Basic Energy Sciences, Catalysis Science program, under grant DE-SC0021955. S.R. acknowledges support from IIT Kanpur (Project number 2024098) and the Chandrakanta Kesavan Center for Energy Policy and Climate Solutions, IITK (Project number 2021136H). A.C.M. would like to acknowledge CONAHCyT for the doctoral scholarship provided under the program (CVU1051087). A.I.F. and S.X. acknowledge support by the NSF grant CHE 2102299. The work carried out at Brookhaven National Laboratory was supported by the DOE under contract DE-SC0012704. XAS measurements used resource 7-BM of the National Synchrotron Light Source II, a DOE Office of Science User Facility operated for the DOE Office of Science by Brookhaven National Laboratory under contract DE-SC0012704. The 7-BM beamline operations were supported in part by the Synchrotron Catalysis Consortium (DOE Office of Basic Energy Sciences grant DE-SC0012335). We appreciate beamline support by L. Ma, D. Yang and A. Tayal. Z.L. would like to thank T. Zhang and X. She for their valuable suggestions.

Author contributions

Z.L. and X.L. conceptualized the project under the supervision of Yayuan Liu; Z.L. synthesized catalysts, performed electrochemical tests, and analyzed experimental data. X.L. synthesized and characterized organic compounds. R.W. performed DFT calculations under the supervision of Yuanyue Liu; C.S.G and Z.L. conducted in situ ATR-SEIRAS measurements under the supervision of V.S.T.; S.R., A.C.M., and P.M.A. performed XPS and TEM characterizations. S.X. and A.I.F. carried out XAS measurements and analyses. L.Z. and K.N.J. conducted SEM characterizations. A.M., D.L., A.L., and L.G. helped with data processing. T.L. carried out ICP-OES measurements. Z.L., X.L., and Yayuan Liu wrote the paper. All authors discussed the results and commented on the paper.

Competing interests

The authors declare no conflict of interest.

Additional information

Supplementary information The online version contains supplementary material available at https://doi.org/10.1038/s41467-025-58593-w.

Correspondence and requests for materials should be addressed to Zhengyuan Li or Yayuan Liu.

Peer review information *Nature Communications* thanks Yafei Li, and the other anonymous reviewer(s) for their contribution to the peer review of this work. A peer review file is available.